Appendix

A. Parameter Settings and Training Details

All models are trained for 50 epochs using the AdamW optimizer, with a cyclical learning rate schedule or a linear warming learning rate schedule. We choose the network width from $\{32, 64\}$ and the number of layers from 2 to 4. The batch size is selected from $\{2, 4, 8\}$. All experiments are conducted on a single NVIDIA A40 GPU.

The $f_{\text{U-Net}}$ model adopts a lightweight U-Net encoder to capture geometric interface information, with the number of encoder layers selected from $\{2, 4\}$.

The f_{FNO} model adopts a single-layer FNO-based encoder and decoder, with the FNO width fixed at 32 and the number of FNO modes selected from $\{8, 16\}$.

To test the performance in the low-data regimes, we conduct downsampling to sample data as training dataset. In the single bubble case, we use a training resolution that is downsampled by a factor of 2 from the original dataset resolution. For the saturated pool boiling case, subcooled pool boiling case, flow boiling gravity case, and 3D pool boiling ISS gravity case, we downsample the original resolution by a factor of 8 to obtain the training resolution. In the super-resolution experiments, we evaluate the models by predicting at 2× and 4× higher resolutions than the training resolution. These evaluation resolutions are obtained by downsampling the original dataset by a factor of 4 and 2, respectively, ensuring that all supervision remains consistent with the ground-truth data from the original high-resolution simulation.

For the single bubble case, the trajectory consists of 500 time steps, of which 450 are randomly selected for training and the remaining 50 for testing. For the 3D pool boiling ISS gravity case, the trajectory consists of 29 time steps, of which 26 are randomly selected for training and the remaining 3 for testing. For other cases with multiple simulation trajectories, one trajectory is randomly reserved for testing, and the remaining trajectories are used for training.

B. Details of the Test Cases

Single Bubble This case provides a fundamental two-dimensional (2D) simulation that isolates the dynamics of a single vapor bubble. It captures the complete lifecycle of the bubble from its inception at a nucleation site on a heated surface to its subsequent detachment and ascent through the liquid. This idealized scenario serves as an essential baseline for understanding and validating more complex multi-bubble systems.

The simulation begins with a bubble forming on the heater. As it grows by evaporation, buoyancy forces increase until they overcome the surface tension forces holding it to the surface, causing it to detach. The case clearly records the velocity and temperature fields surrounding the bubble as it rises and deforms, and visualizes them in Fig. 6.

Boundary Conditions: The domain features a no-slip (Dirichlet) condition on the vertical walls and the heated bottom surface. An outflow (Neumann) condition is applied at the top boundary.

- Side Walls: A no-slip boundary condition is applied, where velocity components are zero. This is a Dirichlet condition: $\vec{u} = (u_x, u_y) = 0$.
- Bottom Heater: A no-slip and constant temperature boundary condition is applied. This is also a Dirichlet condition: $\vec{u} = 0$ and $T = T_{wall}$.
- Top Outflow: A pressure outflow condition is used, where the normal gradients of velocity and temperature are zero. This is a Neumann condition: $\frac{\partial \vec{u}}{\partial n} = 0$ and $\frac{\partial T}{\partial n} = 0$.
- Liquid-Vapor Interface: "Jump Conditions" exist at the interface, where pressure, velocity, and temperature are discontinuous, governed by surface tension and phase change (evaporation).

Initial Conditions: The simulation starts with a quiescent liquid, and a single bubble is initiated at a predefined nucleation site on the heater.

- At $t = 0$, the entire computational domain is filled with a quiescent liquid, with a zero velocity field: $\vec{u}(t = 0, x, y) = 0$.
- The liquid temperature is uniform and equal to the bulk temperature: $T(t = 0, x, y) = T_{bulk}$.
- An initial small bubble nucleus is placed at a predefined nucleation site on the bottom heater surface.

Case Details: This is a single simulation comprising 500 timesteps($\Delta t = 0.5$) with a spatial resolution of 192x288, resulting in a compact 0.5 GB case. Here, Δt represents the temporal resolution in non-dimensional time, which defines the time interval between consecutive frames of the simulation. For the FC-72 fluid used, a Δt of 1 is equivalent to 0.008 seconds of physical time.

Saturated Pool Boiling This case simulates pool boiling under saturated conditions, where the bulk liquid is maintained at its boiling point, known as the saturation temperature (T_{sat}). At this temperature, the liquid is in thermal equilibrium with its vapor phase, and heat addition from the submerged surface leads to vigorous bubble formation (nucleate boiling), a highly efficient mode of heat transfer.

This case captures the transition from an orderly bubbly flow regime at lower heater temperatures to a chaotic, large-scale slug flow as the temperature approaches the Critical Heat Flux (CHF), as visualized in Fig.7. The relationship between the applied heat flux and the wall superheat ($T_{wall} - T_{sat}$) in the simulations has been validated against experimental boiling curves, ensuring physical accuracy.

The primary parameter varied across the 13 simulations in this set is the heater wall temperature, which ranges from 60°C to 120°C.

Boundary Conditions: The domain consists of no-slip (Dirichlet) side walls, a constant temperature heater at the bottom (Dirichlet), and an outflow condition at the top (Neumann).

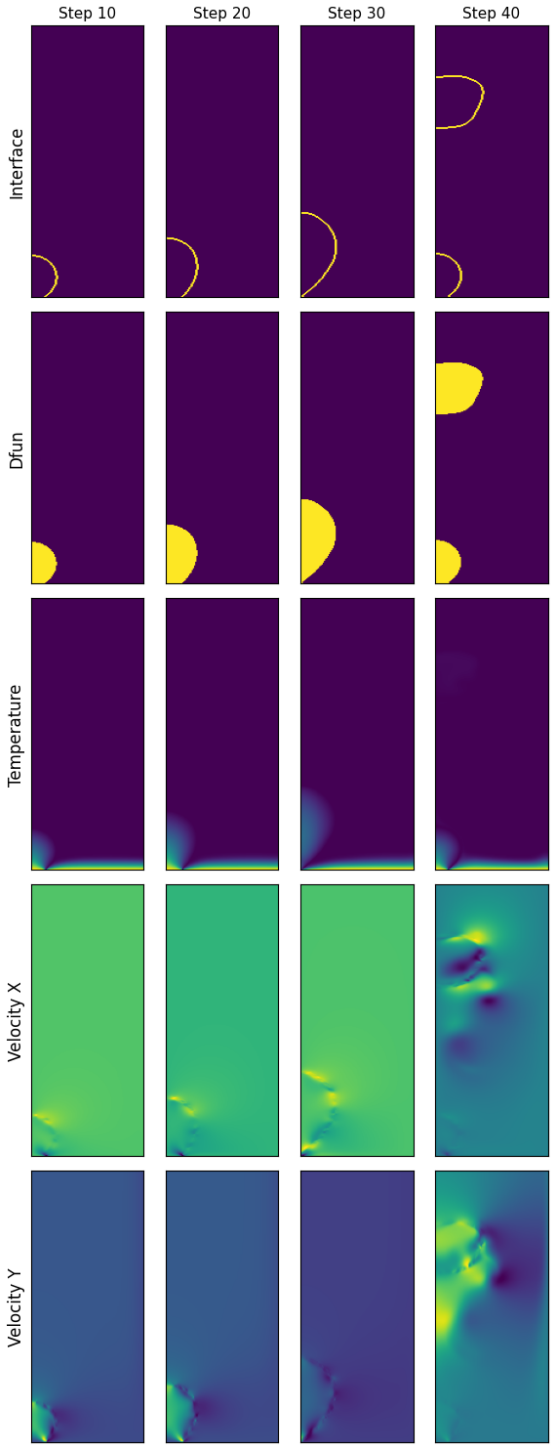

Figure 6: This image visualizes key physical fields from a Single Bubble at four time steps (10, 20, 30, and 40). The rows display the vapor phase (bubbles) via the signed distance function Dfun, which is positive inside the vapor, and the precise bubble interface, located where dfun = 0. The Temperature field is shown in a non-dimensional [0-1] range and illustrates heat transport; The Velocity X & Y fields represent the horizontal and vertical fluid motion induced by the bubble dynamics.

- Side Walls: No-slip condition, a Dirichlet condition: $\vec{u} = 0$.
- Bottom Heater: Constant temperature heater, a Dirichlet condition: $T = T_{wall}$. It is also no-slip: $\vec{u} = 0$.
- Top Outflow: Pressure outflow condition, a Neumann condition: $\frac{\partial \vec{u}}{\partial n} = 0$ and $\frac{\partial T}{\partial n} = 0$.

Initial Conditions: The simulation begins with a quiescent liquid at saturation temperature. Bubbles nucleate from active sites on the heater surface.

- At $t = 0$, the liquid is in a quiescent state: $\vec{u}(t = 0, x, y) = 0$.
- The liquid temperature is equal to the saturation temperature: $T(t = 0, x, y) = T_{sat} = T_{bulk}$.
- Initial bubble nuclei are generated randomly or regularly at multiple predefined nucleation sites on the heater surface.

Case Details: The case consists of 13 simulations, each with 200 timesteps($\Delta t = 1.0$) at a spatial resolution of 512x512, totaling 24.2 GB.

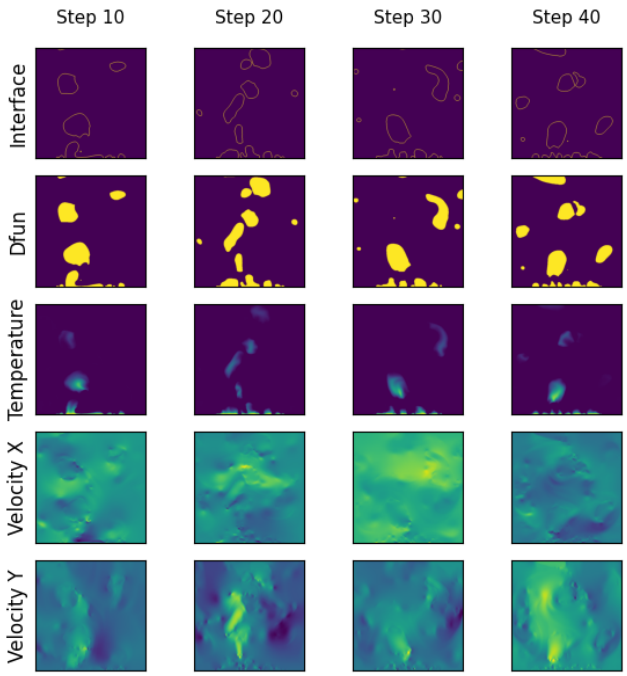

Figure 7: This image visualizes key physical fields from a Saturated Pool Boiling at four time steps (10, 20, 30, and 40).

Subcooled Pool Boiling This case models a more complex boiling scenario where the bulk liquid temperature is below its saturation point ($T_{bulk} < T_{sat}$). This condition leads to the simultaneous occurrence of evaporation at the hot surface and condensation at the bubble's interface with

the colder bulk fluid. Bubbles nucleate and grow within a thin thermal layer adjacent to the heater surface. As they grow and detach, they move into the subcooled liquid, causing them to shrink and collapse due to condensation, as visualized in Fig. 8. This process generates significant turbulence and vortical structures that enhance heat transfer. The varied parameter is the level of subcooling.

Boundary Conditions: The physical setup is identical to the saturated pool boiling case, with no-slip walls, a constant temperature heater, and an outflow top boundary.

Initial Conditions: The simulation starts with a quiescent liquid at a bulk temperature below saturation.

- At $t = 0$, the liquid is in a quiescent state: $\vec{u}(t = 0, x, y) = 0$.
- The liquid temperature is uniform and below the saturation temperature: $T(t = 0, x, y) = T_{bulk} < T_{sat}$.

Case Details: The standard resolution case contains 10 simulations with 200 timesteps($\Delta t = 1.0$) each at a 384x384 resolution (10.3 GB).

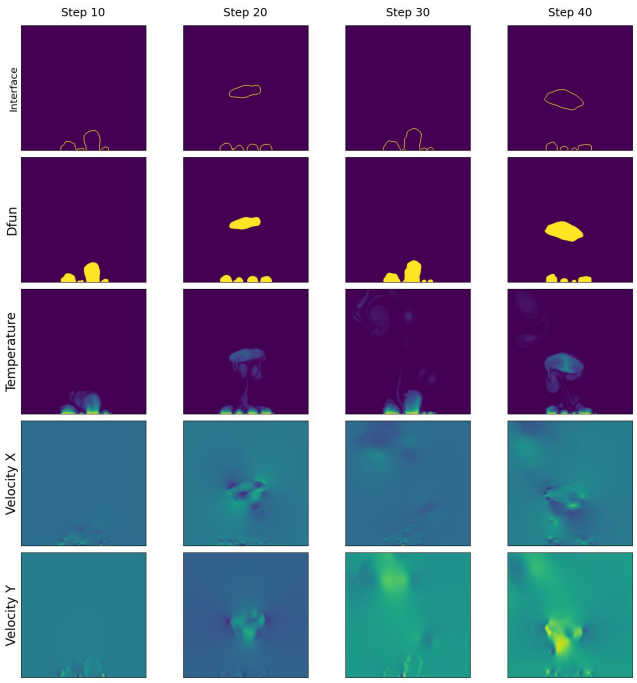

Figure 8: This image visualizes key physical fields from a Subcooled Pool Boiling at four time steps (10, 20, 30, and 40).

Flow Boiling Gravity This case simulates boiling within a fluid flowing through a channel with a heated bottom surface, specifically investigating the influence of varying gravity levels. This scenario is critical for designing thermal management systems for applications in aerospace and microgravity environments, where buoyancy effects are altered. In flow boiling, heat transfer is governed by a combination of forced convection from the imposed flow and buoyant forces acting on the vapor bubbles. Gravity influences bubble trajectory, the propensity for bubbles to rise or stratify, and the transition between different flow regimes, such as bubbly and slug flow, as visualized in Fig. 9. This case explores that interplay under varying gravitational accelerations. The varied parameter is the gravitational acceleration, which is adjusted to simulate conditions from Earth gravity down to microgravity.

Boundary Conditions: The domain features a fluid inlet (Dirichlet), an outlet (Neumann), a no-slip top wall, and a heated bottom section (Dirichlet).

- Left Inlet: A specific velocity profile (e.g., parabolic) is defined, which is a Dirichlet condition: $\vec{u} = \vec{u}_{inlet}$. The temperature is also fixed at $T = T_{bulk}$.
- Right Outlet: A pressure outflow condition is used, which is a Neumann condition: $\frac{\partial \vec{u}}{\partial n} = 0$.
- Top Wall: A no-slip condition is applied, which is a Dirichlet condition: $\vec{u} = 0$.
- Bottom Wall: This boundary is split. The heated section has a constant temperature (Dirichlet $T = T_{wall}$), while the unheated sections are adiabatic (Neumann $\frac{\partial T}{\partial n} = 0$). The entire bottom wall is no-slip (Dirichlet $\vec{u} = 0$).

Initial Conditions: The simulation starts with a steady, single-phase channel flow, after which the heater is activated.

- At $t = 0$, the liquid is in a quiescent state: $\vec{u}(t = 0, x, y) = 0$.
- The liquid temperature is uniform and below the saturation temperature: $T(t = 0, x, y) = T_{bulk} < T_{sat}$.

Case Details: The standard resolution case has 6 simulations with 200 timesteps($\Delta t = 1.0$) at a 1600x160 resolution (10.9 GB).

3D Pool Boiling ISS Gravity This case provides a three-dimensional (3D) simulation of pool boiling in a microgravity environment, simulating the conditions aboard the International Space Station (ISS). In such an environment, the effects of buoyancy are significantly diminished, and surface tension becomes the dominant force. This completely alters the dynamics of bubble growth, merger, and departure, which is critical for the design of phase-change heat transfer systems in aerospace applications.

This simulation captures the unique phenomena of Surface Tension Dominated Boiling (SDB). Unlike on Earth where bubbles detach periodically, in microgravity, a large "central bubble" forms and remains on the heater surface, acting as a "vapor sink" for smaller, surrounding satellite bubbles. The case clearly visualizes the size fluctuations of this central bubble due to the balance between evaporation and condensation, along with the complex vortical structures that result.

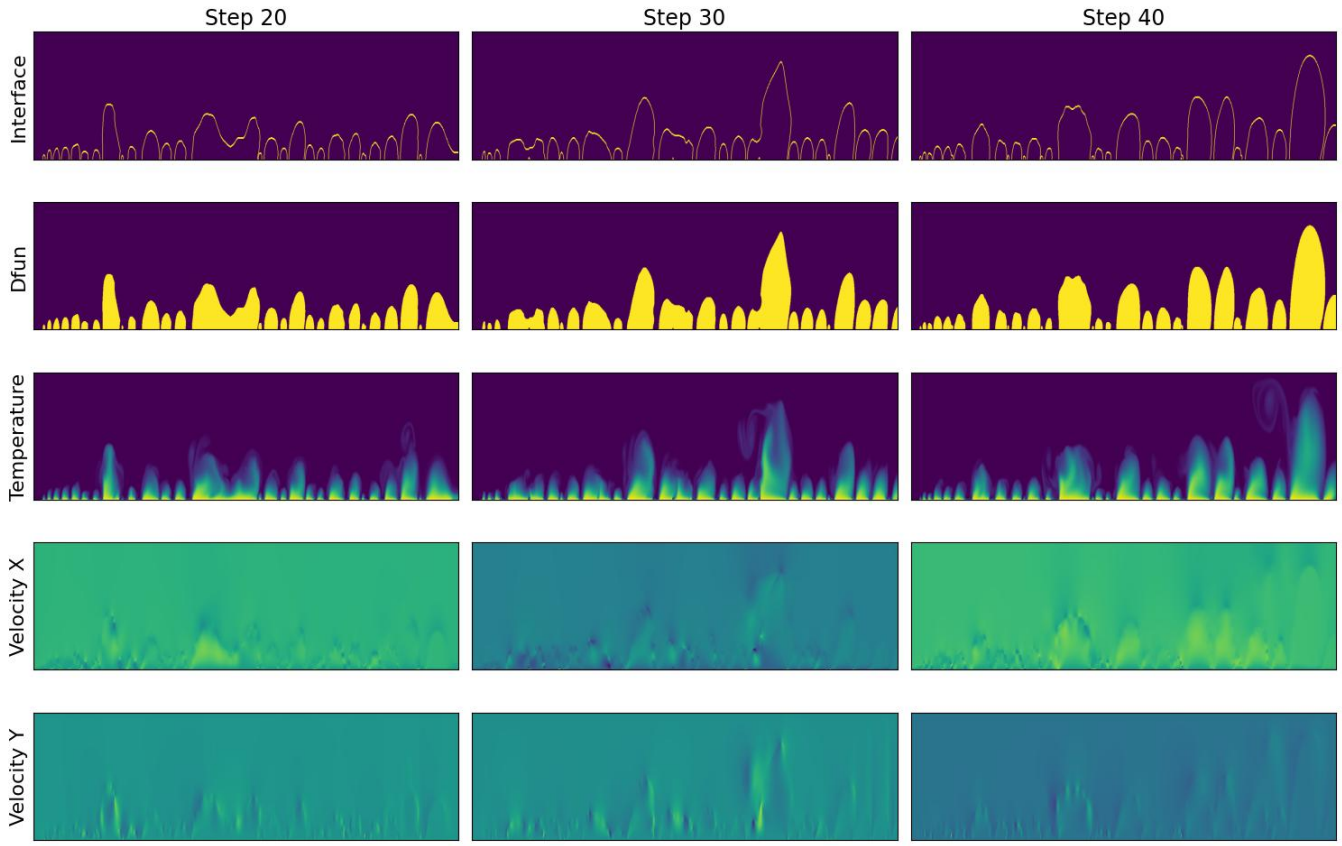

Figure 9: This image visualizes key physical fields from a Flow Boiling Gravity at three time steps (20, 30, and 40).

This case represents a specific case within a broader gravity-scaling study, with its gravity parameter set to simulate the microgravity environment of the ISS to explore the physics of surface-tension-dominated boiling.

Boundary Conditions: The simulation domain features no-slip side walls, a constant-temperature heated bottom surface, and a pressure outflow top surface.

- **Side Walls:** A no-slip boundary condition is applied, where all velocity components are zero. This is a Dirichlet condition: $\vec{u} = (u_x, u_y, u_z) = 0$.
- **Bottom Heater:** A no-slip and constant temperature boundary condition is applied. This is also a Dirichlet condition: $\vec{u} = 0$ and $T = T_{\text{wall}}$.
- **Top Outflow:** A pressure outflow condition is used, where the normal gradients of velocity and temperature are zero. This is a Neumann condition: $\frac{\partial \vec{u}}{\partial n} = 0$ and $\frac{\partial T}{\partial n} = 0$.
- **Liquid-Vapor Interface:** "Jump Conditions" exist at the interface, where pressure, velocity, and temperature are discontinuous, governed by surface tension and phase change (evaporation).

Initial Conditions: The simulation begins with a quiescent, subcooled liquid, and bubbles are initiated at nucleation sites on the heater surface.

- At $t = 0$, the entire computational domain is filled with a quiescent liquid, with a zero velocity field: $\vec{u}(t = 0, x, y, z) = 0$.
- The liquid temperature is uniform and below the saturation temperature: $T(t = 0, x, y, z) = T_{\text{bulk}} < T_{\text{sat}}$.
- An initial small bubble nucleus is placed at a predefined nucleation site on the bottom heater surface.

Case Details: This is a single simulation comprising 29 timesteps ($\Delta t = 1.0$) with a spatial resolution of $400 \times 400 \times 400$, resulting in a 62.6 GB case.

The key symbols used are defined in Table 2.

C. Rollout Prediction Performance

Table 3 presents the rollout prediction results for multiple physical fields (T, u_x, u_y) on a subcooled pool boiling case, evaluated using both RMSE and IRMSE metrics. Lower values for both RMSE and IRMSE indicate better performance. Our proposed method, IANO, is compared against several baseline neural operators: MIONet, U-Net, CODA-NO, and GNOT.

Symbol	Description	Definition / Context
T_{wall}	Wall Temperature	A constant temperature applied to the heater surface (Dirichlet condition).
T_{bulk}	Bulk Temperature	The initial temperature of the bulk liquid, away from the heat source.
T_{sat}	Saturation Temperature	The boiling point of the liquid, where it is in thermal equilibrium with its vapor.
Δt	Temporal Resolution	The non-dimensional time interval between consecutive simulation frames.
D_{fun}	Signed Distance Function	A function to visualize the vapor phase; positive for vapor, negative for liquid.
$\vec{u}_{\text{inlet}}$	Inlet Velocity	A specified velocity profile applied at the channel inlet in the flow boiling case .
CHF	Critical Heat Flux	Acronym for the limit where heat transfer efficiency sharply degrades.

Table 2: Nomenclature for symbols.

Fields	Metric	MIONet	U-Net	CODA-NO	GNOT	IANO
T	RMSE	0.052	0.064	0.062	0.153	**0.045**
	IRMSE	0.173	0.190	0.192	0.347	**0.167**
u_x	RMSE	0.271	0.295	0.304	0.700	**0.248**
	IRMSE	0.695	0.723	0.701	1.212	**0.668**
u_y	RMSE	0.286	0.313	0.347	0.841	**0.258**
	IRMSE	0.570	0.588	0.627	0.790	**0.540**

Table 3: The rollout prediction results of multiple fields on the Subcooled Pool Boiling case.

As presented in Table 3, across all evaluated physical quantities and metrics, the IANO model consistently achieved the best performance. Specifically, for temperature (T) prediction, IANO's RMSE was 0.045, markedly outperforming MIONet (0.052), U-Net (0.064), CODA-NO (0.062), and GNOT (0.153). Its IRMSE also recorded the lowest value at 0.167, indicating superior accuracy in the interface regions. For x-direction velocity (u_x), IANO's RMSE was 0.248, again lower than all other models, with its IRMSE of 0.668 maintaining the lead. In predicting y-direction velocity (u_y), IANO once more demonstrated the top performance, with an RMSE of 0.258 and an IRMSE of 0.540. The above results indicate that our method can also achieve superior prediction accuracy in a rollout manner.

D. Details of Super-Resolution Performance

We present an analysis of our proposed IANO method's performance in super-resolution physical field prediction. We compare IANO against established baseline neural operators: MIONet, U-Net, CODA-NO, and GNOT. All models are trained on 1x resolution datasets and then evaluated at 1x, 2x, and 4x resolutions, where 2x and 4x indicate test data resolutions that are two and four times, respectively, that of the training data. Performance is measured using RMSE and IRMSE for the temperature field (T), X-direction velocity field (u_x), and Y-direction velocity field (u_y). The detailed results are summarized in Table 4.

The experimental data unequivocally shows IANO consistently achieves the leading prediction accuracy across all tested resolutions (1x, 2x, 4x) and for all physical field prediction tasks (T, u_x, u_y). Even at the training resolution (1x), IANO establishes a superior baseline. For instance, in temperature field prediction, IANO's RMSE is 0.030 and its IRMSE is 0.118, outperforming U-Net (0.035, 0.129) and MIONet (0.046, 0.160).

IANO's advantages become particularly pronounced when predicting at higher super-resolution factors (2x and 4x). For the 4x super-resolution task on the temperature field (T), IANO's RMSE remains exceptionally low at 0.031, with its IRMSE only slightly increasing to 0.132. In contrast, U-Net's RMSE significantly rises to 0.060, and CODA-NO's to 0.059, with corresponding increases in IRMSE. Even the robust GNOT model, with an RMSE of 0.037 and IRMSE of 0.163 at 4x resolution, still falls short of IANO's precision.

A similar trend is observed for the velocity fields. For u_x at 4x super-resolution, IANO records the lowest RMSE of 0.152 and IRMSE of 0.605. Similarly, for u_y at 4x resolution, IANO maintains the lowest RMSE (0.155) and a highly competitive IRMSE (0.520). This forms a clear performance gap compared to models like U-Net and CODA-NO, which experience more substantial accuracy degradation at increased resolutions. It's also worth noting that MIONet does not provide results for 2x and 4x super-resolution tasks, implicitly highlighting its limitations in handling resolution-enhancement scenarios and further underscoring IANO's versatility and robustness.

This consistent superior performance, especially as resolution increases, demonstrates IANO's remarkable ability to effectively learn and reconstruct high-frequency details from lower-resolution inputs. This capability is crucial for accurately capturing the intricate dynamics of physical fields and maintaining precision, even when data is sparse or requires upsampling.

Fields	Resolution	MIONet		U-Net		CODA-NO		GNOT		IANO	
		RMSE	IRMSE	RMSE	IRMSE	RMSE	IRMSE	RMSE	IRMSE	RMSE	IRMSE
T	1x	0.046	0.160	0.035	0.129	0.036	0.134	0.037	0.139	**0.030**	**0.118**
	2x	–	–	0.057	0.175	0.040	0.160	0.037	0.158	**0.031**	**0.130**
	4x	–	–	0.060	0.179	0.059	0.194	0.037	0.163	**0.031**	**0.132**
u_x	1x	0.225	0.670	0.183	0.647	0.197	0.674	0.208	0.644	**0.173**	**0.629**
	2x	–	–	0.213	0.682	0.195	0.685	0.199	0.648	**0.162**	**0.637**
	4x	–	–	0.228	0.677	0.215	0.691	0.194	0.614	**0.152**	**0.605**
u_y	1x	0.216	0.521	0.162	0.479	0.175	0.501	0.213	0.491	**0.146**	**0.459**
	2x	–	–	0.226	0.578	0.193	0.554	0.215	0.523	**0.155**	**0.509**
	4x	–	–	0.267	0.637	0.238	0.604	0.217	0.534	**0.155**	**0.520**

Table 4: Super-resolution evaluation on the Subcooled Pool Boiling case. MIONet, whose branch networks rely on fixed sampling locations, does not support super-resolution, hence results are only available at $1\times$ resolution.

Noise level	MIONet		U-Net		CODA-NO		GNOT		IANO	
	RMSE	IRMSE	RMSE	IRMSE	RMSE	IRMSE	RMSE	IRMSE	RMSE	IRMSE
1%	0.486	1.351	0.381	1.261	0.405	1.300	0.439	1.307	**0.364**	**1.219**
3%	0.496	1.357	0.386	1.253	0.416	1.312	0.446	1.281	**0.378**	**1.233**
5%	0.510	1.364	0.400	1.253	0.417	1.318	0.438	1.286	**0.383**	**1.223**

Table 5: The prediction results of the Subcooled Pool Boiling case under noisy data.

E. Details of Robustness under Noisy Data

This section analyzes the noise robustness of our proposed IANO method against baseline neural operators (MIONet, U-Net, CODA-NO, GNOT) in predicting all fields on the subcooled pool boiling case. We evaluate model performance across various noise levels (1%, 3%, and 5%) introduced into the training data. Performance is quantified using Root Mean Squared Error (RMSE) for overall prediction accuracy and Interface Root Mean Squared Error (IRMSE) for accuracy specifically at interfaces. The detailed results are presented in Table 5.

The experimental results clearly demonstrate that IANO consistently outperforms all baseline methods across every tested noise level, achieving the lowest RMSE and IRMSE values. Even with 1% noise, IANO records an RMSE of 0.364 and an IRMSE of 1.219, showing superior performance compared to the next best, U-Net (RMSE 0.381, IRMSE 1.261).

As the noise level increases to 3% and 5%, IANO maintains its leading position, further highlighting its exceptional robustness. At 5% noise, IANO's RMSE is 0.383 and its IRMSE is 1.223. While all models exhibit a slight increase in error with rising noise, IANO's error increase is notably smaller, maintaining a substantial performance gap. For instance, at 5% noise, IANO's RMSE is still considerably lower than U-Net's (0.400), CODA-NO's (0.417), and MIONet's (0.510).

This consistent superiority under noisy conditions underscores IANO's remarkable ability to effectively filter out noise and learn meaningful physical patterns from perturbed data. This robustness is critical for real-world applications where training data is often imperfect or contains inherent measurement noise, making IANO a highly reliable tool for scientific computing in challenging environments.

F. Details of Ablation Studies.

This section presents the results of an ablation study evaluating the contributions of key components within our full model ("Ours") to the prediction of temperature (T) and velocity ($\vec{u}$) fields. We analyze three ablated variants: "w/o Inter. Encoding" (without Interface-Aware Multiple Functions Encoding), "w/o Geo. Encoding" (without Geometry-Aware Positional Encoding), and "w/o Interface" (without explicit interface data). Performance is measured using RMSE (Root Mean Squared Error) for overall accuracy and IRMSE (Interface Root Mean Squared Error) for accuracy at interfaces, across four multiphase flow cases: subcooled pool boiling (Subcooled), flow boiling gravity (Gravity), saturated pool boiling (Saturated), and single bubble (Single).

The results in Table 6 consistently show that our full model achieves the best performance across all cases and metrics, demonstrating its robust design. Specifically, removing the Geometry-Aware Positional Encoding ("w/o Geo. Encoding") leads to the most significant performance degradation, particularly evident in the IRMSE. For instance, in the Subcooled case, the IRMSE jumps from 1.206 to a substantial 1.630, and in the Saturated case, it increases from 1.260 to a striking 1.901. This highlights the critical role of precise geometric context in accurately capturing complex field behaviors, especially at interfaces.

The absence of explicit interface data ("w/o Interface") also consistently impairs performance. We see noticeable increases in RMSE and IRMSE across most cases. For example, RMSE rises from 0.519 to 0.550 for Gravity, and

Model	Subcooled		Gravity		Saturated		Single	
	RMSE	IRMSE	RMSE	IRMSE	RMSE	IRMSE	RMSE	IRMSE
IANO	0.349	1.206	0.519	0.811	0.761	1.260	0.128	0.287
w/o Inter. Encoding	0.360	1.212	0.534	0.818	0.812	1.305	0.132	0.286
w/o Geo. Encoding	0.378	1.630	0.534	0.831	0.861	1.901	0.130	0.290
w/o Interface	0.363	1.235	0.550	0.855	0.826	1.331	0.128	0.284
w/o Inter. Encoding and Interface	0.380	1.249	0.541	0.845	0.858	1.363	0.130	0.291

Table 6: The performance comparison of all ablated algorithms.

Model	RMSE (w/o Inter.)	RMSE (with Inter.)	Difference	IRMSE (w/o Inter.)	IRMSE (with Inter.)	Difference
MIONet	1.107	1.134	-2.43%	1.543	1.559	-1.03%
GNOT	1.006	1.004	$+0.20\%$	1.463	1.440	$+1.58\%$
IANO	**0.826**	**0.761**	$\mathbf{+7.83\%}$	**1.331**	**1.260**	$\mathbf{+5.31\%}$

Table 7: Performance comparison with and without interface data across various models on the Saturated Pool Boiling case.

IRMSE increases from 1.260 to 1.331 for Saturated. This underscores the value of directly incorporating interface information for both overall and interface-specific accuracy.

In addition, removing the Interface-Aware Multiple Functions Encoding ("w/o Inter. Encoding") results in a milder, yet consistent, performance reduction across various scenarios. For instance, the RMSE for Subcooled increases from 0.349 to 0.360, and for Saturated, it goes from 0.761 to 0.812. This confirms its contribution to the model's ability to effectively learn and integrate multiple input functions.

Finally, Table 7 evaluates the impact of incorporating interface data on the predictive performance of different models. A positive percentage in the "Difference" columns indicates an improvement when interface data is utilized. Our method, IANO, demonstrates a substantial performance gain with the inclusion of interface information, showing an impressive 7.83% improvement in RMSE and a 5.31% improvement in IRMSE. This clearly highlights IANO's effective leveraging of interface data for enhanced prediction accuracy. In contrast, MIONet exhibits a decline in performance with interface data, with RMSE worsening by 2.43% and IRMSE by 1.03%. GNOT shows a marginal improvement of 0.20% in RMSE and 1.58% in IRMSE, which is significantly less pronounced than IANO's gains. This suggests that while MIONet and GNOT can use interface data, their architectures lack the specialized modules necessary to effectively model the intricate coupled relationships between the physical fields and the topological positions of the interfaces, leading to negligible improvement or even degradation.

In summary, this ablation study clearly validates that each specialized component within our proposed model is crucial. The Geometry-Aware Positional Encoding and the explicit Interface data contribute most significantly to enhancing accuracy, particularly at critical interface regions, while the Interface-Aware Multiple Functions Encoding further refines the model's overall robustness.

G. More Numerical Result Visualization and Computational Cost

In this section, we present the visualization results of IANO and several baseline models on the subcooled pool boiling and single bubble cases. Overall, our model, IANO, comprehensively outperforms all compared methods, particularly in predicting the bubble locations. In Fig. 10, which visualizes the subcooled pool boiling case, the temperature and velocity fields generated by IANO demonstrate a remarkable degree of agreement with the ground truth. Benefiting from the high-frequency information at the interface locations, it accurately captures the morphological details of the plumes and the fine vortex structures within the flow field. In contrast, the performance of other models is lacking. For instance, U-Net's results appear blurry, while GNOT and CODA-NO, despite showing improvement, still render details too smoothly, failing to fully reproduce the true complexity of the physical process. This superior performance is further confirmed in the single bubble scenario shown in Fig. 11. IANO's predictions are nearly a perfect replica of the ground truth, whereas the prediction images from MIONet and U-Net are filled with destructive grid-like noise and artifacts. While GNOT's results are good, they still exhibit a slight gap in fidelity compared to IANO.

In the error visualizations for the single bubble scenario, presented in Fig. 12, the quantitative results are clear. The explicitly labeled Root Mean Square Error (RMSE) values show that IANO achieves the lowest error across all three physical quantities—temperature, X-velocity, and Y-velocity. Its advantage in precision is overwhelming; for example, its temperature error is merely one-third of GNOT's and one-sixth of U-Net's. But this is not the whole story. The spatial distribution of the error reveals the true core advantage of the IANO method. In fluid dynamics, the most challenging regions to simulate, characterized by the most drastic changes, are the interfaces between different media. Observing the error maps for U-Net and GNOT, it is evident that their errors are concentrated precisely along these critical interface boundaries. The shape of the error almost out-

Model	FLOPs (M)
MIONet	8
U-Net	811
CODA-NO	6514
GNOT	10242
IANO	3270

Table 8: The computational cost of all compared algorithms

lines the flow's contour, indicating that these models fail in the most crucial physical regions. In stark contrast, IANO's error map appears as a uniform pale color across the entire domain, even at the most challenging interface locations, which visually demonstrates its extremely low error. This decisively demonstrates the effective utilization of interface information in IANO's model design, enabling it to deeply understand and master the complex dynamics of the interface regions, thereby overcoming the bottlenecks common to other models.

We calculate the computational cost for the subcooled pool boiling case, and the analysis represented by Floating Point Operations (FLOPs) in Table 8 shows that compared to several advanced neural operators such as CODA-NO and GNOT, our proposed IANO model has significantly reduced computational burden, requiring 1.586 billion FLOPs. Although MIONet exhibits the lowest computational cost at 8 million FLOPs, its accuracy often lags behind IANO, while IANO achieves a commendable balance between its excellent predictive performance and reasonable computational efficiency, making it a feasible solution for complex multiphase flow simulations.

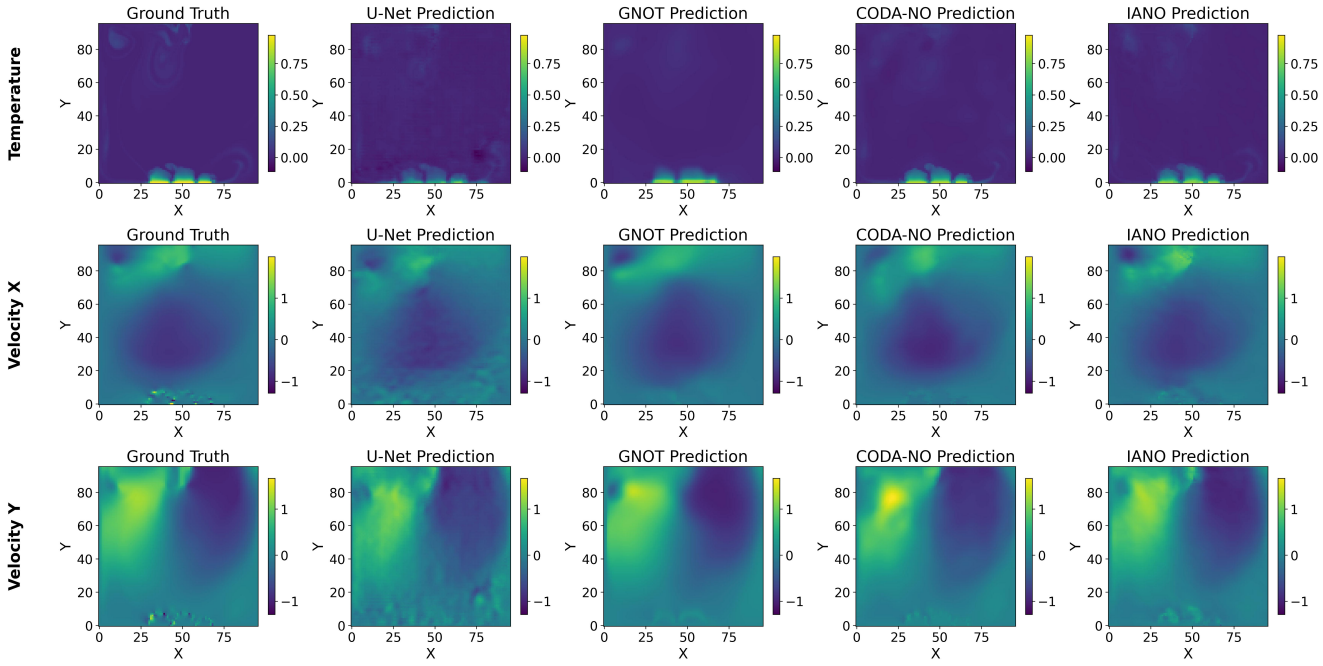

Figure 10: The 2× super-resolution prediction results for Subcooled Pool Boiling, with MIONet omitted due to lack of support

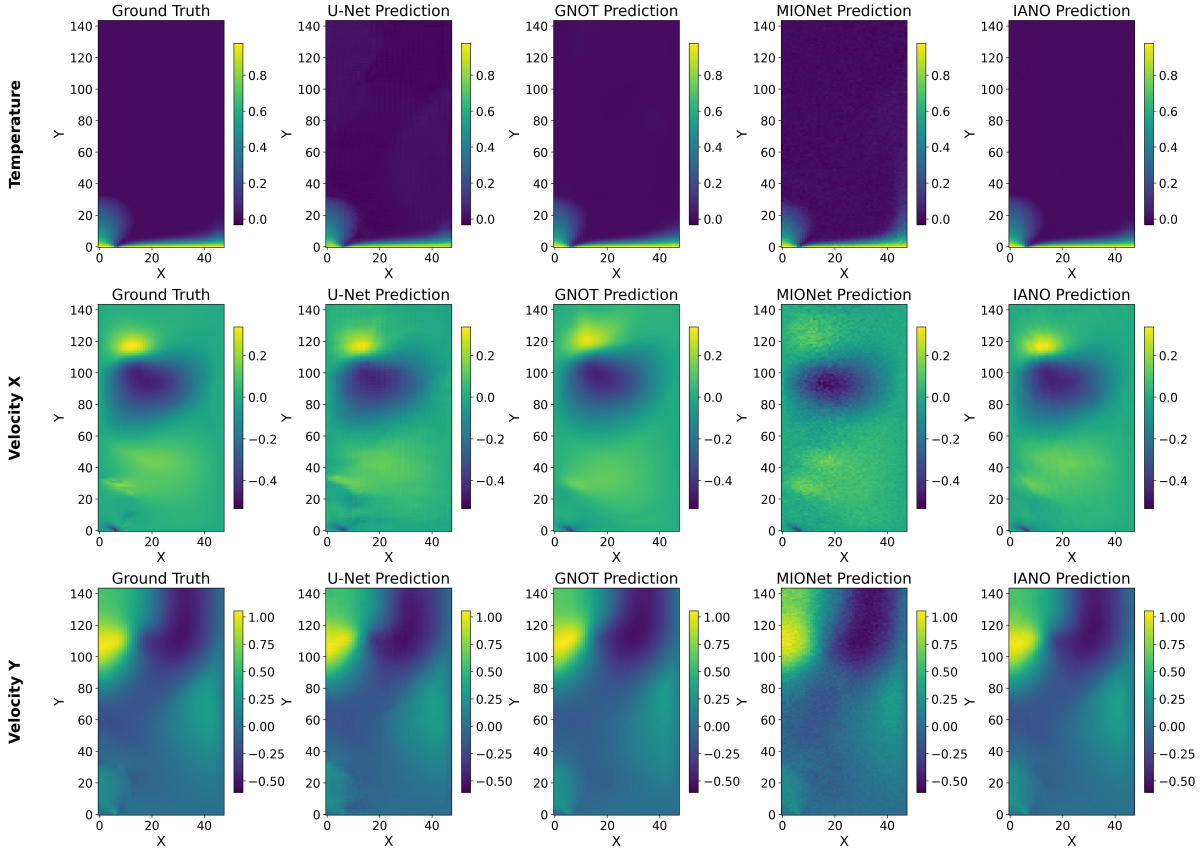

Figure 11: Prediction visualized on the Single Bubble case. CODA-NO is missing due to unstable training and failure.

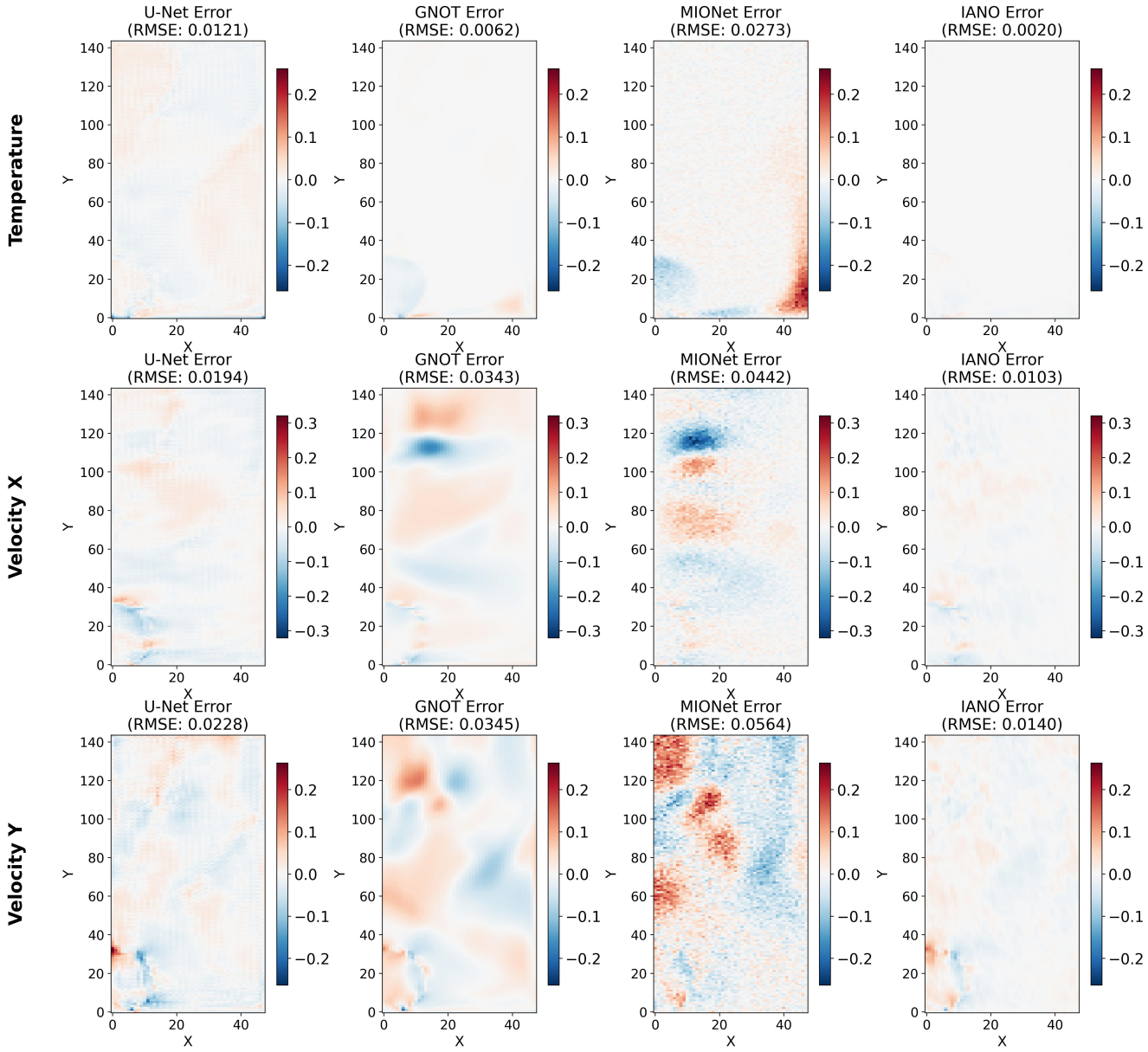

Figure 12: Error visualized on the Single Bubble case. CODA-NO is missing due to unstable training and failure.